Modeling a High-Power RF System Using a Circuit Optimizer

M. Taquet, S. Chicarella, H. Damerau, A. Jibar, A. Lasheen, M. Morvillo, *Member, IEEE*, J. M. Redouté, *Senior Member, IEEE*, and C. Rossi

***Abstract*—The increasing demand for higher beam intensities to reach higher luminosities puts significant stress on high-power amplifiers driving the RF cavities in particle accelerators. It is therefore essential to understand their large signal behavior in detail. The need to characterize the high-power nonlinear amplifiers of the 80 MHz RF systems of the CERN proton synchrotron (PS) at the circuit level, including their distributed and stray components, only accessible for a limited amount of time due to accelerator operation, led us to develop a novel modeling approach. It is based on low-power and high-power measurements, as well as a numerical circuit optimizer. This allowed us to build a model that replicates the beam-cavity interaction across the entire dynamic range of the system with good agreement between simulations and measurements. Furthermore, observations indicate that the three 80 MHz RF systems interact differently with the beam. The model was used to identify the specific components responsible for these distinct beam–cavity interactions, and provides valuable insights into the components responsible for the potential limitations of the amplifier chain.**

***Index Terms*—Beam-cavity interaction, circuit model, high-power radio frequency (RF) amplifier, RF measurements.**

I. Introduction

RADIO frequency (RF) systems in particle accelerators provide the power to change the energy of a charged particle beam. A typical RF system includes a resonant structure, the RF cavity, inside which the longitudinal electric field is established. The power is delivered by one or several power amplifiers, driven by a low-level RF (LLRF) system [1]. A configuration used in many accelerators worldwide combines one or more low-power solid-state amplifiers with one or more high-power vacuum tube amplifiers to deliver hundreds of kilowatts of power to the RF cavity and to the beam (e.g., [2], [3], [4]). Due to their large power range, the vacuum tube amplifiers may create nonlinear effects that can affect the system's performance, especially for high beam intensities [3], [5]. To accurately model such effects, a common approach is to realize a lumped element circuit model of the amplifiers, which is effective for frequencies up to about 10 MHz [3], [6], [7]. However, as the frequency, the size of the circuit, and the number of amplification stages increase, it becomes more and more complex to model the system at the circuit level, mainly due to the presence of stray and distributed components. The case of the 80 MHz RF systems of the CERN proton synchrotron (PS) led us to develop a new modeling approach, based on low-power and high-power measurements, as well as a circuit optimizer.

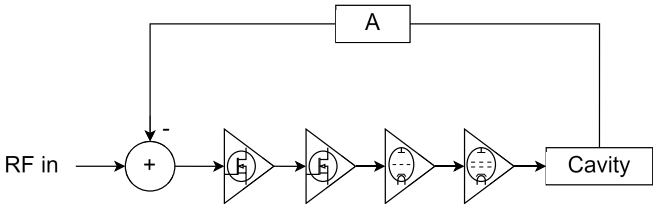


Fig. 1. Block diagram of the 80 MHz amplifier chain. The parameter A represents the total attenuation of the feedback path. The RF in is the signal generated by the LLRF, allowing the 300 kV cavity voltage to be obtained after amplification by the four stages.

The 80 MHz RF systems of the CERN PS comprise three RF cavities (named C80-88, C80-89, and C80-08), each connected to a chain of four amplifiers. The first two stages in the chain, the summing amplifier and the pre-driver, are solid-state amplifiers. The last two stages, the driver and the final amplifier, consist of high-power RF vacuum tubes. As represented in Fig. 1, each cavity is equipped with a wideband feedback to reduce its beam induced voltage [8].

For proton operation, two cavities are requested to deliver the nominal peak RF voltage of 300 kV per cavity to the beam in a 300 μs pulse [9]. This pulse is provided just prior to ejection from the PS in order to fit the bunches into the short buckets of the 200 MHz RF system of the super proton synchrotron (SPS) [10]. As no real power is transferred to the beam through this manipulation, the beam current behaves as a purely reactive time varying load for the final amplifier [11], and the cavity is equipped with a tuning system to compensate for this additional load. However, due to the presence of the wideband feedback, the amplifiers must deliver higher average RF power to the cavity under beam loading conditions, even if there is no acceleration. Therefore, higher beam intensities may give rise to potential limitations of the amplifier chain. It is essential to evaluate these limitations, especially in the context of the increasing demand for higher intensity and

Received 8 January 2026; revised 15 May 2026; accepted 23 June 2026. Date of publication 1 July 2026; date of current version 18 August 2026. This work was supported by the Organization Européene Pour la Recherche Nucléaire (CERN). *(Corresponding author: M. Taquet.)*

M. Taquet is with the Linacs, Injector Synchrotrons Section, CERN, 1211 Geneva, Switzerland, and also with the Department of Electrical Engineering and Computer Science, University of Liège, 4000 Liège, Belgium (e-mail: mathieu.florent.taquet@cern.ch).

S. Chicarella, A. Jibar, M. Morvillo, and C. Rossi are with the Linacs, Injector Synchrotrons Section, CERN, 1211 Geneva, Switzerland.

H. Damerau and A. Lasheen are with the Beams and RF Studies Section, CERN, 1211 Geneva, Switzerland.

J. M. Redouté is with the Department of Electrical Engineering and Computer Science, University of Liège, 4000 Liège, Belgium.

Color versions of one or more figures in this article are available at https://doi.org/10.1109/TNS.2026.3709061.

Digital Object Identifier 10.1109/TNS.2026.3709061

© 2026 The Authors. This work is licensed under a Creative Commons Attribution 4.0 License.
For more information, see https://creativecommons.org/licenses/by/4.0/

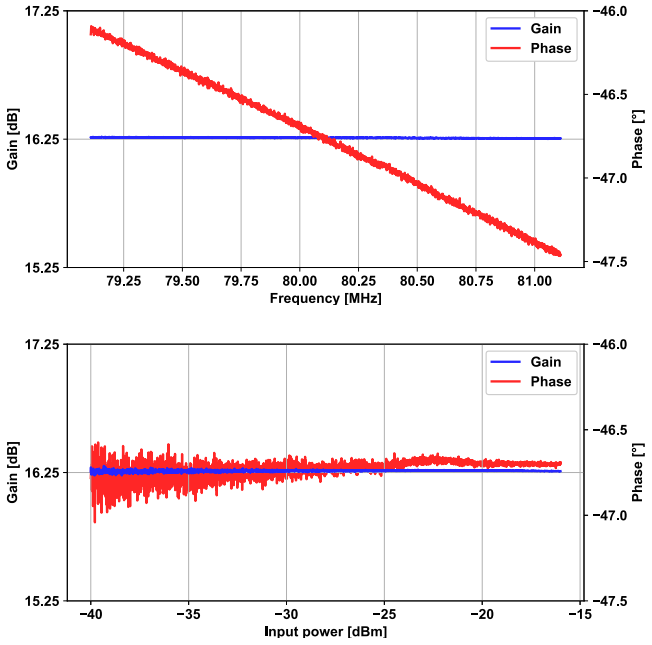


Fig. 2. Measurement of the S_{21} parameter of the summing amplifier as a function of frequency (top). The magnitude of S_{21}, the gain, is stable (blue) over the whole bandwidth of the system, and the phase is linear (red). It is also constant as a function of power over the dynamic range of the device (bottom).

brightness beams with projects such as the high luminosity large hadron collider (HL-LHC), which consequently required an upgrade of the injector chain [12], [13].

In order to address this challenge, a detailed circuit model of the 80 MHz RF system was developed. As a practical example, the RF system of the cavity C80-88 was considered in detail for the model development. Dedicated measurements were performed to establish the power and frequency dependent amplifier responses, in order to determine what level of complexity was needed to model each of them. For the amplifiers that were modeled at the component level, a numerical circuit optimizer was employed to minimize the difference between simulations and measurements. With this approach, the model reached an excellent correspondence with experiments. It allows, for example, to determine the parameters responsible for the observation that the different 80 MHz RF systems interact with the beam in distinct ways [14] and to identify the parameters requiring a proper adjustment. Eventually, the model is exploited to identify the intensity limitations of each component of the chain.

II. Solid-State Amplifiers

A. Summing Amplifier

The aim of the summing amplifier is to combine the LLRF drive signal and the portion of the cavity gap voltage re-injected into the chain, as required by the wideband feedback. This is achieved with a 3 dB power combiner followed by an amplification stage based on a solid-state integrated circuit. As the summing amplifier is a low-power device, with 0 dBm of nominal output power, the complete set of scattering parameters can be measured with a vector network analyzer (VNA) for its full characterization [15]. Two different measurements

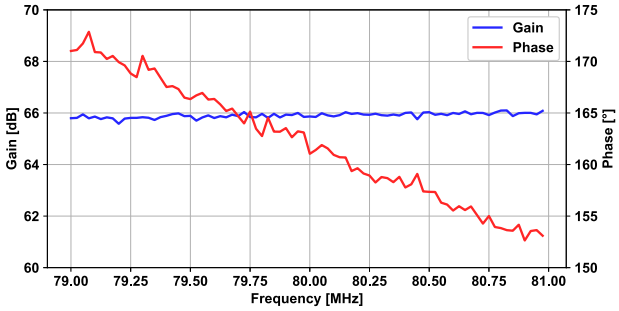


Fig. 3. Measured pre-driver low-power gain (blue) and phase (red) as a function of frequency.

are conducted: a frequency sweep over the 80 MHz system's bandwidth $\Delta f \approx 1$ MHz and a power sweep at the nominal frequency of $f_{\mathrm{rf}} = 80.11$ MHz, up to the nominal output power of the device. The measurement of the S_{21} parameter (see Fig. 2) shows that the amplifier has constant gain over the full power and frequency range. Therefore, it can be modeled as a constant gain and delay block, and the measurement of its S_{21} parameter is sufficient for its characterization.

B. Pre-driver Amplifier

Like the summing amplifier, the pre-driver amplifier was measured using the VNA with a frequency and a power sweep. The low-power measurement shows that the pre-driver gain varies by less than $\pm$ 0.2 dB in the relevant bandwidth with a linear phase behavior (or constant delay, see Fig. 3). Therefore, its gain is considered to be constant as a function of frequency.

Due to its 2 kW nominal output power, the characterization of the pre-driver in the high-power regime requires modifying the measurement setup. The 66 dB gain of the amplifier at low-power requires the addition of significant attenuation at its output. In addition, the device must be gated to reduce the average power [16]. This allows to measure the output voltage amplitude V_{out} at f_{rf}, depicted in Fig. 4. The measurement shows that even though the pre-driver gain is constant with frequency, it is power dependent.

Therefore, it was modeled as a nonlinear voltage block, obtained by fitting the measured V_{out} with an odd polynomial function of the RF input voltage amplitude V_{in}, i.e.,

$$V_{\mathrm{out}} = \sum_{k=0}^{n} a_{2k+1} V_{\mathrm{in}}^{2k+1}. \tag{1}$$

III. Tube Amplifiers

Both vacuum tube amplifiers change their characteristics over their power range. Therefore, they were modeled at the component level, in the low-power and high-power regimes.

Moreover, since these stages directly impact the longitudinal beam coupling impedance, their detailed understanding is crucial. However, the modeling of the vacuum tube based amplifiers is subject to several additional complications.

1) Due to the parasitic elements of the driver amplifier, which cannot be neglected at 80 MHz, the schematic is insufficient to model the measured behavior.
2) The final stage contains distributed components and does not have any associated schematic.

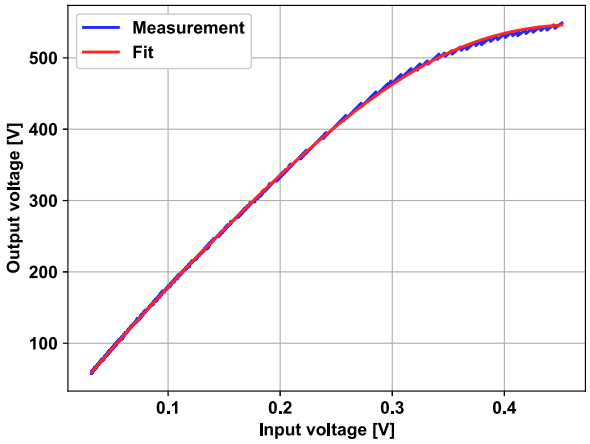


Fig. 4. Output voltage of the pre-driver as a function of its input voltage over the power range of the amplifier.

3) The driver and final amplifiers are both installed in the accelerator tunnel, with very limited access, which excludes a long series of measurements.

As a result of those constraints, the values of the components of the circuits are not perfectly known a priori. Therefore, the low-power representation was modeled with the software AWR Microwave Office [17]. It was chosen for its built-in optimizer feature, which can be employed to adjust the values of the circuit components by minimizing the difference between simulations and measurements. Indeed, among the features available in AWR Microwave Office are the `SDeltaM` and `SDeltaP` functions, which can be, respectively, employed to quantify the magnitude and phase differences between any measured and simulated S parameters over a specified frequency range. These quantities can be defined as optimization goals, allowing the software to automatically adjust the circuit components' values according to the chosen optimization variables and algorithm. This approach is particularly useful in a large scale system where an analytical description of the response (e.g., [6]) is impractical. The use of a circuit optimizer allows generic optimization of lumped elements and transmission line models without any additional analytical modeling.

The high-power vacuum tube models have been realized with PSpice [18]. For the low-power representation, the nonlinear tube amplifiers are replaced by their small signal model. The tubes transconductance and anode resistance [19], [20] are extracted from the I–V curves of the tubes datasheets at the relevant bias points. Therefore, the AWR simulations are performed using linearized tube models comprising a controlled current source with a gain equal to the transconductance, together with the anode resistance and the inter-electrode capacitances. When moving to the high-power case with PSpice, the small signal models of the tubes must be modified to large signal models. They were built by fitting the I–V curves of the datasheets. This generic method, applicable for a constant screen grid voltage, described in [21], expresses the anode current, I_A, of the tubes in the following way:

$$I_A\left(V_A, V_{gc}\right) = A_n\left(V_A\right) V_{gc}^n + A_{n-1}\left(V_A\right) V_{gc}^{n-1} + \ldots + A_1\left(V_A\right) V_{gc} + A_0\left(V_A\right). \quad (2)$$

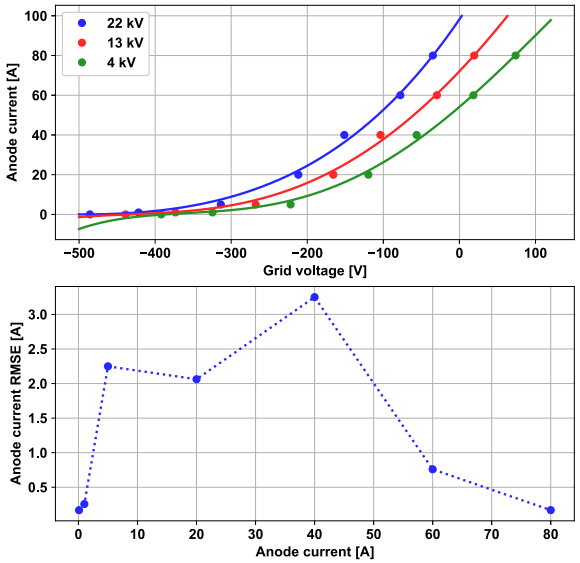


Fig. 5. Top plot corresponds to the datasheet points of the tube TH681 (dots) together with the curves obtained with fourth order polynomials, for different anode voltages. The RMSE of the anode current associated with these three curves is represented in the bottom plot.

Here, V_A represents the tube anode voltage and V_{gc} the grid to cathode voltage. First, a set of $k+1$ polynomials with coefficients $a_{n,\ldots,0,k,\ldots,0}$ is calculated by fitting the data sheet values of the anode current with (2) for $k+1$ constant values of the anode voltage. The coefficients $A_i(V_A)$ are obtained by linearly interpolating between the coefficients $(a_{i,k}, a_{i,k-1}, \ldots, a_{i,0})$, where i varies from 0 to n.

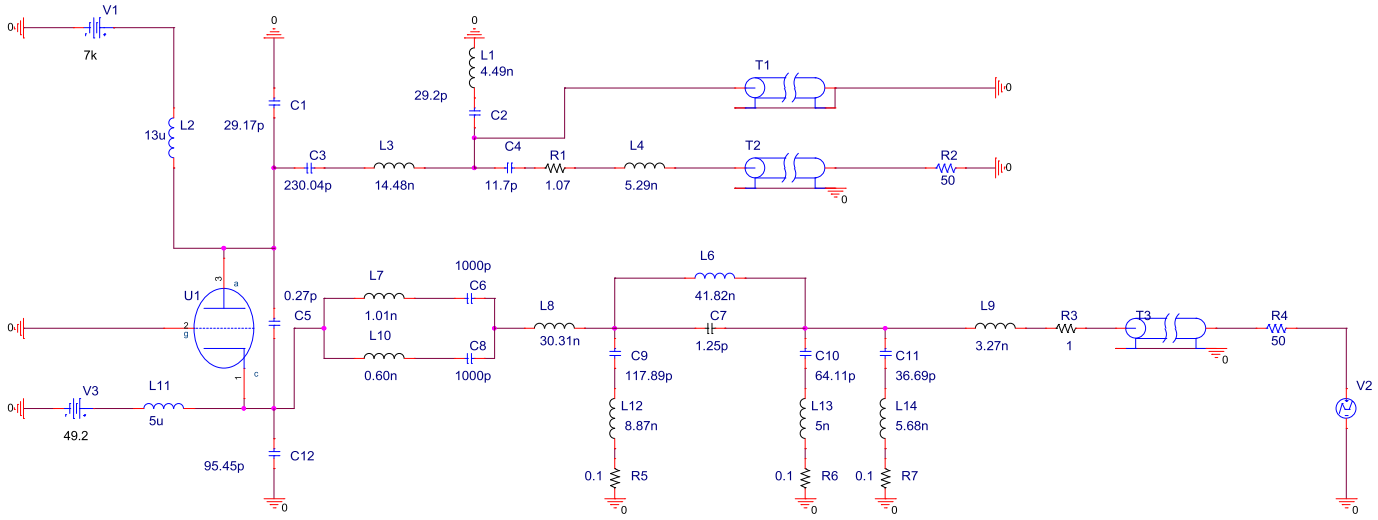
For illustration, the datasheet points of the anode current of the final amplifier tube, the Thales tetrode TH681, have been fit with fourth-order polynomials. This polynomial order provided the best compromise in the present case. Indeed, lower order polynomials lead to fit curves that do not represent the physical behavior of a vacuum tube, especially at low grid voltages, while higher order polynomials introduce overfitting effects. The top plot of Fig. 5 shows the comparison between the fit curves and the datasheet I–V characteristics for different anode voltages. The associated root mean square error (RMSE) is also provided on the bottom plot to quantify the fitting accuracy.

A. Driver Amplifier

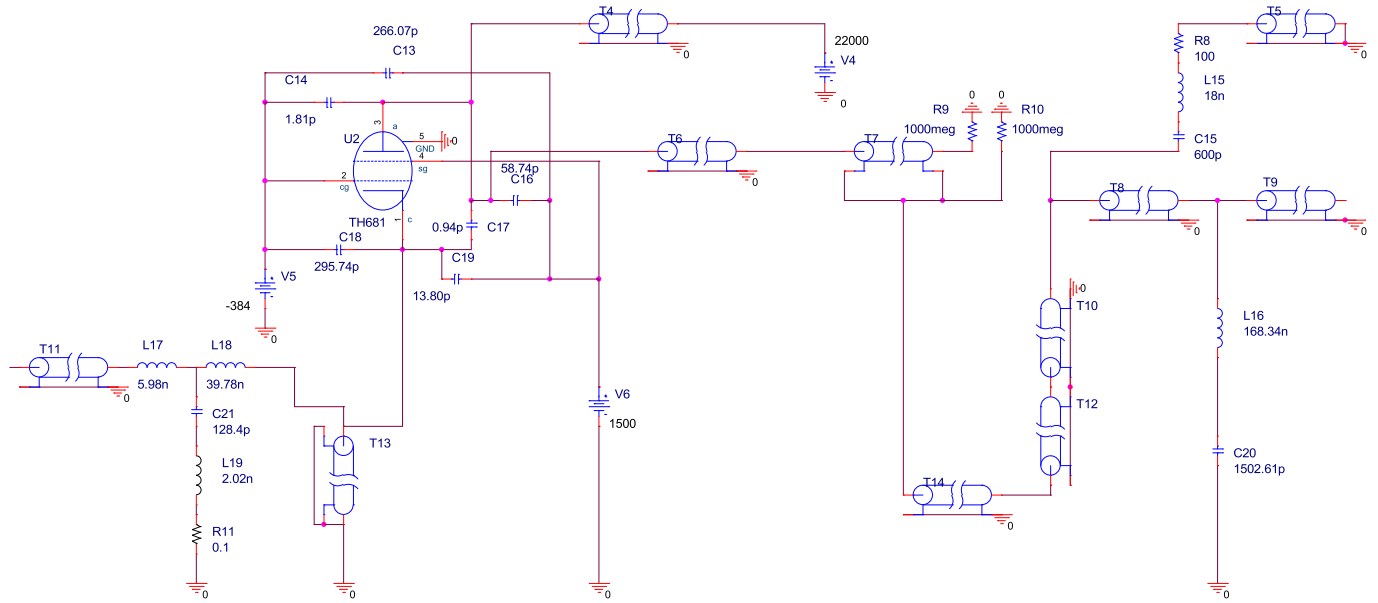
The driver amplifier [see Fig. 6(a)] is a single-stage amplifier based on the Eimac triode 3CPX5000A7 in the grounded-grid configuration. It delivers approximately 40 kW of nominal output power into a 50 Ω load.

Its input circuit consists of a π-shape impedance matching network with two capacitive and one inductive branches. Its output is made of a resonant circuit comprising two capacitors and a transmission line. In the considered frequency range, the stray components of the capacitors and inductors present in the driver must be taken into account. The equivalent models of the capacitors and inductors can be found in [22] and [23]. For clarity purposes, all stray components in the circuits of Fig. 6 were sketched in black.

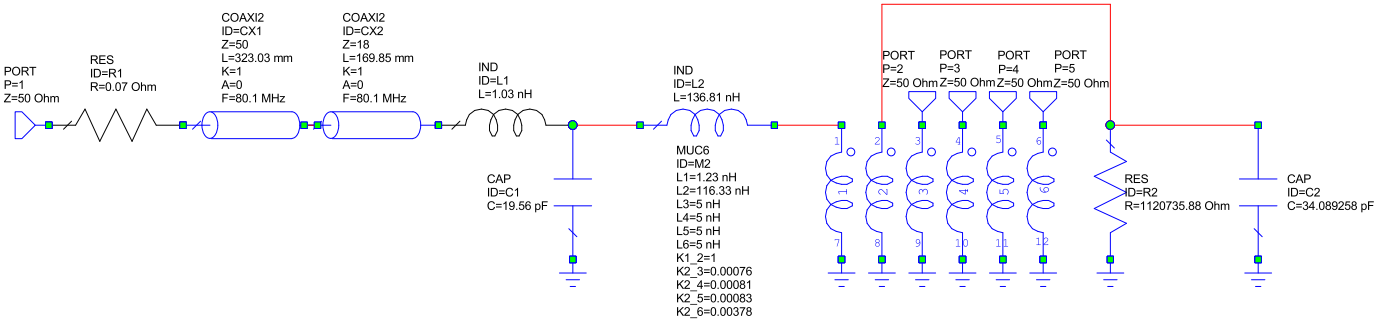
Unlike the two solid-state stages, the scattering parameters of the driver vary significantly over the system's bandwidth



(a)



(b)



(c)

Fig. 6. 80 MHz RF system vacuum tube amplifiers circuit model. (a) Circuit model of the PS 80 MHz RF system driver. The voltage source V2 is connected to the driver input, and its output is connected to the resistor R2. (b) Circuit model of the PS 80 MHz RF system final amplifier. The transmission lines T11 and T9 are present at the input and output of the circuit, respectively. (c) Circuit model of the PS 80 MHz RF system cavity. Port 1 denotes the input port.

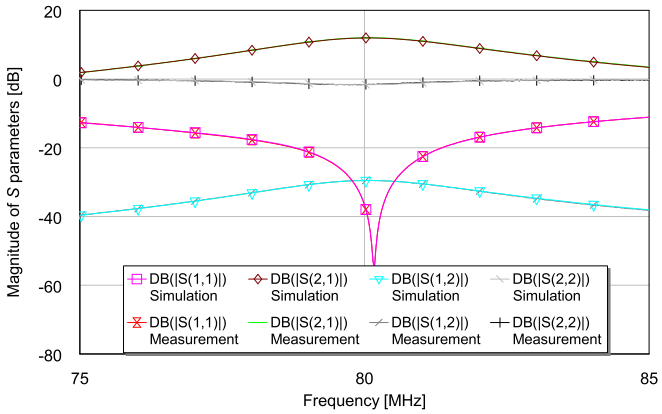


Fig. 7. PS 80 MHz RF system driver low-power characteristics. The simulations and measurements of the scattering parameters are in excellent agreement.

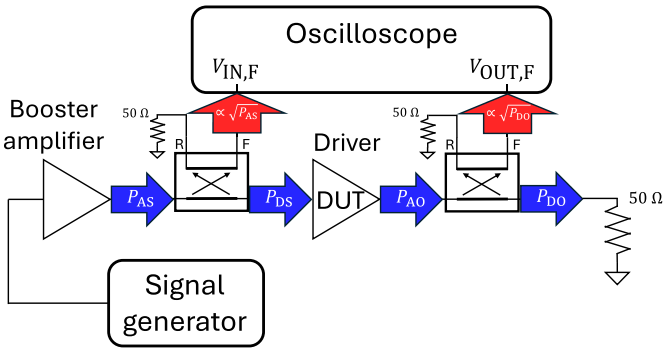


Fig. 8. PS 80 MHz RF system driver amplifier high-power measurement setup. The signal generator sends the input pulse to the pre-driver, which acts as a booster amplifier. The power is swept to cover the dynamic range of the driver amplifier, which is the device under test. Two directional couplers have been inserted to measure the forward voltages in the time domain.

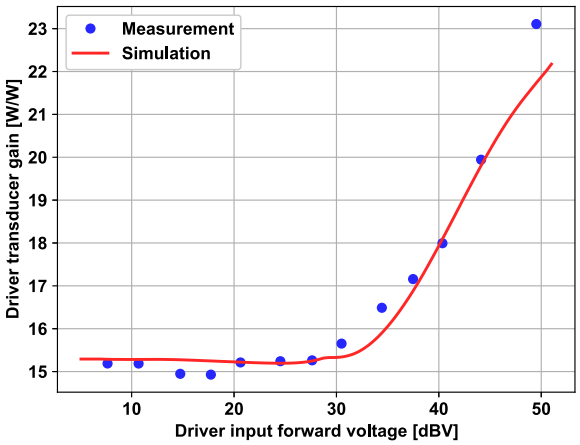


Fig. 9. PS 80 MHz RF system driver transducer gain as a function of its forward input voltage.

for any given power level. Therefore, the complete set of scattering parameters must be taken as a basis for the modeling in the low-power regime. The numerical circuit optimization method has been employed to minimize the `SDeltaM` and `SDeltaP` functions for each port such that the refined driver circuit reproduces the measured scattering parameters. As can be observed in Fig. 7, the measurements are in excellent agreement with the simulations.

To check the validity of the high-power model of the driver, the variation of its transducer power gain at the RF frequency as a function of its input forward voltage has been measured with the setup shown in Fig. 8. The transducer gain G_T is the ratio between the delivered power from the amplifier's output P_{DO} and the available power from the source P_{AS} [24], i.e.,

$$G_T = \frac{P_{\mathrm{DO}}}{P_{\mathrm{AS}}} = \frac{P_{\mathrm{AO}} - P_{\mathrm{L,OUT}}}{P_{\mathrm{DS}} + P_{\mathrm{L,IN}}}. \tag{3}$$

Here, the parameters P_{AO} and P_{DS} are the available power from the amplifier's output and the delivered power from the source, respectively. The power loss due to the input and output mismatch is $P_{\mathrm{L,IN}}$ and $P_{\mathrm{L,OUT}}$.

Since the output directional coupler is terminated with a 50 Ω load, the transducer gain can be expressed as a function of the forward voltage of the input and output couplers at the RF frequency, $V_{\mathrm{IN,F}}$ and $V_{\mathrm{OUT,F}}$, i.e.,

$$G_T\left(V_{\mathrm{IN,F}}\right) = \left(\frac{C_{\mathrm{OUT,F}} V_{\mathrm{OUT,F}}}{C_{\mathrm{IN,F}} V_{\mathrm{IN,F}}}\right)^2. \tag{4}$$

Here $C_{\mathrm{OUT,F}}$ and $C_{\mathrm{IN,F}}$ represent, respectively, the forward voltage coupling of the output and input directional couplers at the RF frequency. As the output of the directional couplers is measured in the time domain, $V_{\mathrm{IN,F}}$ and $V_{\mathrm{OUT,F}}$ are calculated with Fourier analysis. The measurement points are obtained by sweeping the signal generator power to modify $V_{\mathrm{IN,F}}$, and the gain is calculated following (4).

For the simulation, a sinusoidal voltage source at the RF frequency of amplitude $2V_{\mathrm{IN,F}}$ is connected at the input of the driver, through a 50 Ω load, as depicted in Fig. 6(a). This ensures that the simulated input forward voltage is $V_{\mathrm{IN,F}}$. It is swept in amplitude to cover the dynamic range of the amplifier. The simulated curve is obtained by separating the simulation of the input and output forward voltages in different time frames with a Hamming window [25]. For the time frame considered, the ratio of the input and output forward power is calculated. As can be seen in Fig. 9, the model is able to reproduce the variation of the power gain as a function of the input forward voltage of the driver amplifier with an average RMSE of 0.67 over the power range.

B. Final Amplifier

The final amplifier [see Fig. 6(b)] is a single-stage amplifier, rated to deliver 400 kW of nominal output power.

The final amplifier's input is made of an *LC* network in parallel with a tunable stub connected to the cathode of the tetrode. The anode RF voltage is transferred to its output through coaxial transmission lines. The transition of the last 18 Ω output line is modeled as a capacitor to ground connected to the bare cavity through a magnetic coupling loop [see Fig. 6(c)]. The magnetic coupling loop is modeled by a transformer together with a series inductance representing its self-inductance. The secondary winding of this transformer corresponds to the main cavity inductance, which is part of the equivalent *RLC* circuit representing the bare cavity resonance. In addition, this main inductance is weakly coupled to other

inductances, in order to model the pickups of the cavity. The coupling factors are sketched in Fig 6(c).

To characterize the small signal behavior of the final stage, a specific approach was used. The input impedance and the voltage gain of the final amplifier were measured with the VNA (together with the gain between the input and the final amplifier anode pickup). A direct measurement of the output reflection coefficient would have required an appropriate high-power circulator, a directional coupler, and the associated transition elements to protect the instrument [26]. Hence, to characterize the output behavior of the final stage, alternative measurements were performed, taking advantage of the available voltage pickups in the cavity. The measurements of the variation of the quality factor and resonance frequency of the cavity, obtained by measuring the transmission in between the pickups, for different loads connected to the input of the final stage allow to model the output behavior of the system. The open circuit, the 50 Ω, and the short circuit cases were measured. To account for these three different cases, the input port value can be defined as a variable. It can be set to represent the input load. Each case will lead to different expressions of the `SDeltaM` function, which can be optimized simultaneously. As sketched in Fig. 10, the numerical circuit optimization method can be employed to find the optimal values of the circuit components, allowing for reproducing those measurements.

In order to decrease the number of optimization variables of the stage, the cavity, represented in Fig. 6(c), was characterized separately. An appropriate adapter was installed to replace the power amplifier that had been physically disconnected from the cavity.

The input impedance of the cavity can be measured by connecting the VNA to the adapter. To model the coupling of the cavity to its input load, the cavity quality factor and resonance frequency have been measured with the different loads connected at the input of the adapter. Hence, the input port of the cavity was also modeled as a variable. The results of the measurements, in excellent agreement with the simulations obtained with the optimized circuit, can be seen in Fig. 11. The figure also shows that the measurements were performed over different frequency ranges. This was necessary because the cavity has a high quality factor, requiring a narrow bandwidth for precise measurements, while its resonant frequency is affected by the impedance connected to the input port. In order to simultaneously minimize the error between simulations and measurements over these different frequency ranges, the errors associated with the open and short circuit cases were implemented as output equations in AWR. These quantities could then be optimized in the same manner as the `SDeltaM` and `SDeltaP` functions used for the 50 Ω case.

The high-power characterization of the final stage requires another measurement setup in order to provide sufficient power to the amplifier. The nonlinear behavior of the longitudinal beam coupling impedance of the complete system has been measured [14] and can be employed to characterize the final amplifier since the other stages have been modeled.

IV. Complete System

The only element of the diagram in Fig. 1 that remains to be modeled in the small signal regime is the feedback path. For that purpose, the loop gain of the system has been evaluated by measuring the ratio of the open loop to the closed loop gain in the small signal regime. The simulated quality factor and the loop gain at the central frequency $GA(f_{rf})$ are in good agreement (see Fig. 12), and the cavity input has been characterized (see Fig. 11).

Hence, the loaded low-power shunt resistance of the cavity with wideband feedback R_{cl} will also be correctly reproduced.

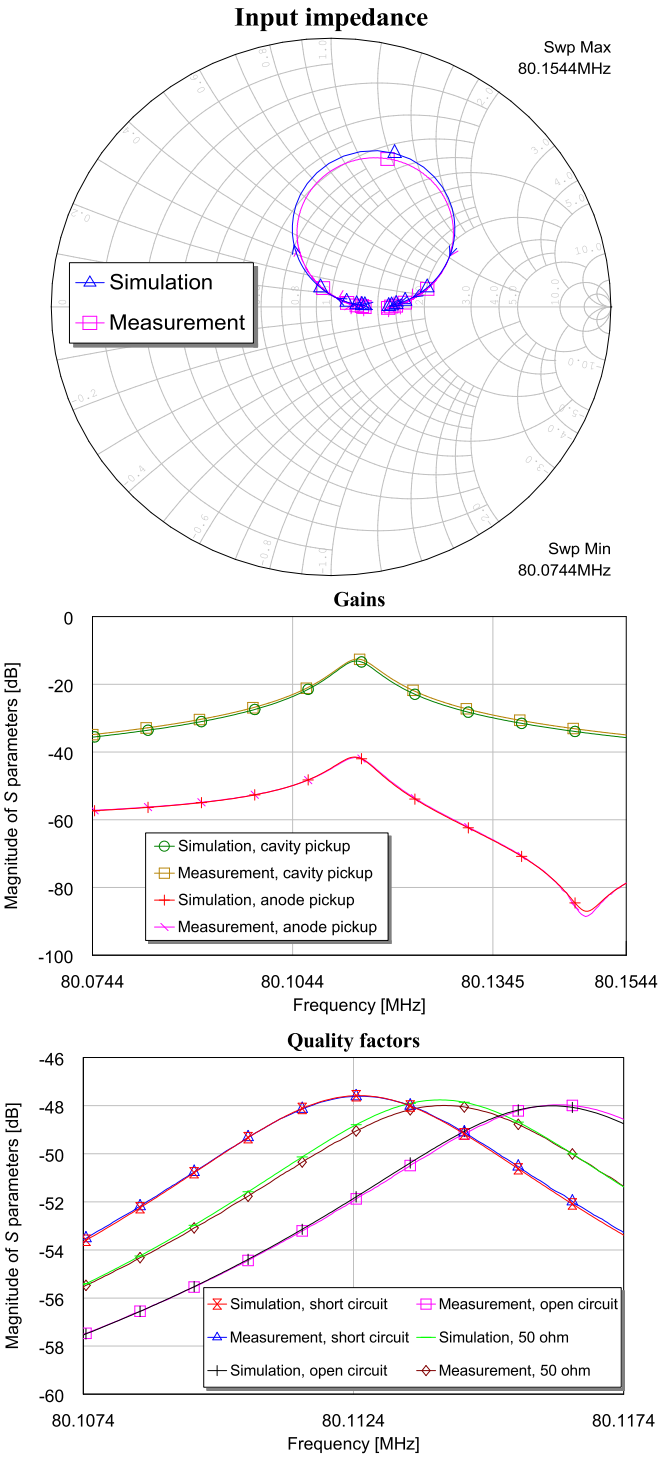


Fig. 10. Final amplifier low-power characteristics. The comparison between the simulations and measurements for the input impedance (top), the gains (middle), and the quality factors (bottom) is in good agreement.

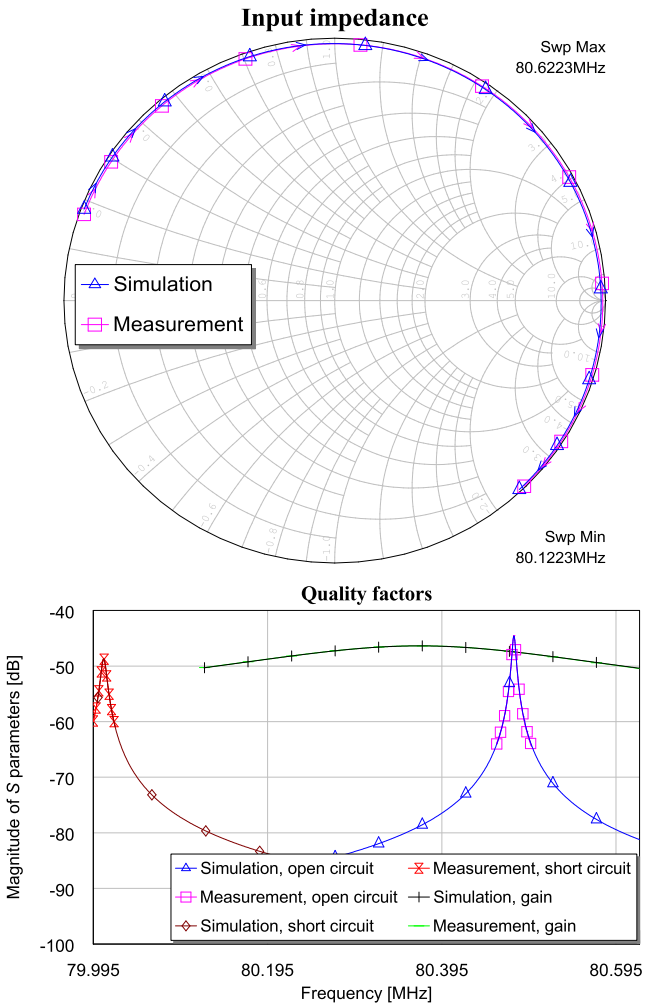


Fig. 11. Characterization of the cavity. The model reproduces the cavity input impedance (top) together with its response for different loads connected to its input (bottom).

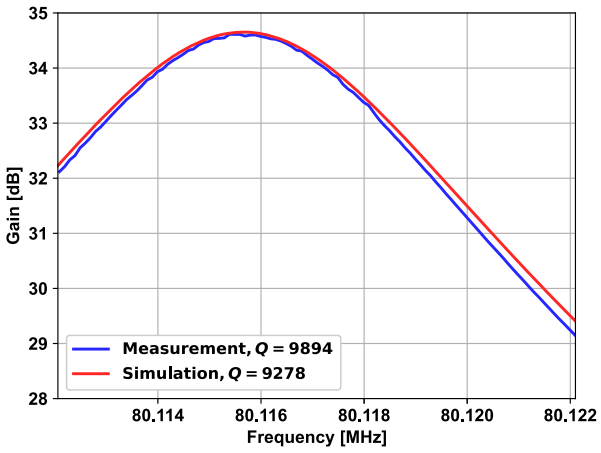


Fig. 12. Measured (blue) and simulated (red) loop gain of the complete system.

This follows from [8]:

$$R_{\mathrm{cl}} = \left| \frac{Z(f_{\mathrm{rf}})}{1 + GA(f_{\mathrm{rf}})} \right| \tag{5}$$

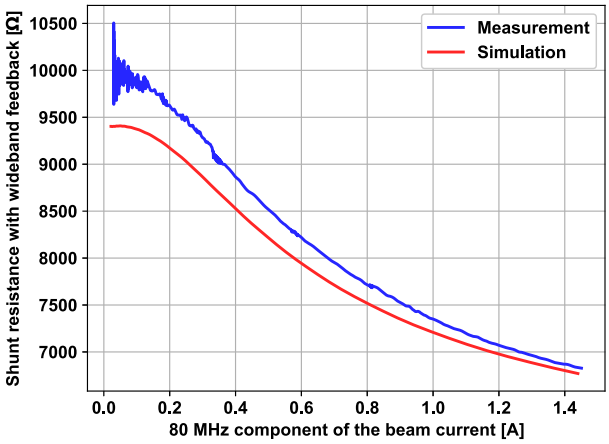


Fig. 13. Measured (blue) and simulated (red) shunt resistance with wideband feedback of the PS 80 MHz RF system as a function of beam current.

where $Z(f_{\mathrm{rf}})$ is the loaded cavity shunt impedance at the RF frequency. It can be directly related to the measured quality factor and the input impedance of the cavity [27].

The high-power behavior of the complete system is simulated by connecting a sinusoidal current source at the RF frequency to the cavity as an input for the simulation. The amplitude of the beam current is swept to reach approximately 1.4 A, corresponding to the maximum RF beam current measured in [14]. For each time frame, the ratio of the Fourier transforms of the cavity voltage and the beam current is calculated, following the same methodology employed for the driver. As can be seen in Fig. 13, the model built with the circuit optimizer is able to reproduce the beam-cavity interaction even at high-power, with an average RMSE of 459 Ω across the complete beam current range, and can thus serve as a basis for proposing solutions to the issues raised in the introduction.

V. Applications of the Simulation Model

A. Coupling Factor Adjustments

As a practical application, the model was applied to determine that three elements were responsible for the different behavior that is observed in the cavities C80-88 and C80-89 of the PS ring under beam loading conditions.

1) The cavity is sensitive to the input circuit of the final amplifier due to the imperfect reverse isolation of the tetrode.
2) The driver amplifier does not have a 50 Ω output source impedance.
3) The line length between the driver and the final amplifier is different for the two systems.

For these reasons, the line length transforms the impedance between the final amplifier cathode and the driver anode, which impacts the coupling to the cavity. This behavior can be observed through the loaded quality factor Q_L [27]. Indeed, Fig. 14 shows that it is possible to obtain a loaded quality factor that is similar to the one measured on the cavity C80-89 ($Q_L \simeq 27\,500$) by modifying the line length between the driver and the final amplifier in the model of the cavity C80-88. Therefore, the length of the line can be modified in

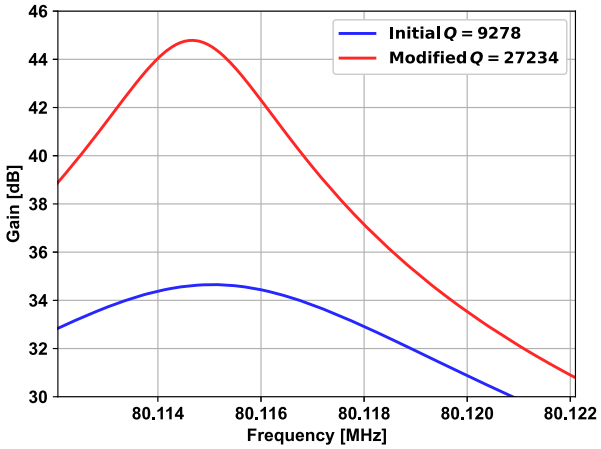


Fig. 14. Simulation of the variation of the PS 80 MHz RF system loop gain for different line lengths between driver and final amplifier. The line length explains the factor of three difference in the loaded quality factor measured between the two cavities.

order to couple the cavities to their amplifier chains in the same way.

B. Limitations Due to Beam Loading

If an element of the chain is experiencing limitations due to beam loading, it would exhibit a compression of its gain. This effect could be identified on the longitudinal beam coupling impedance, according to (5). Indeed, as depicted in Fig. 13, the shunt resistance in the presence of the wideband feedback measured with the beam decreases as the beam current increases. Equation (5) implies that this occurs if the overall gain of the chain is increasing. Consequently, the behavior of the impedance shows that even with an amplitude of the RF beam current of I_b = 1.4 A, no compression effect is visible. The system would reach its limit if the shunt resistance with wideband feedback starts to increase because of the amount of beam current driving the cavity.

Therefore, the impedance measurement technique developed in [14] can be extended to estimate the power limitations of an RF acceleration system. This method has the advantage that the LLRF drive signal is disabled during the measurements, such that the amplifier chain behavior can be analyzed without modeling the LLRF part. One of the main functions of the LLRF system is to control the amplitude of the cavity gap voltage by driving the amplifier chain. Hence, disabling the LLRF implies that the RF system does not provide any voltage to the cavity, and that the cavity voltage is generated solely by the beam. The measurement was performed during a portion of the machine cycle in which the cavity C80-88 normally delivers voltage. However, the required beam structure could still be maintained because other RF systems in the PS provided the necessary voltage.

The principle of the technique is the following. Two real-time signal analyzers measure the time evolution of the RF spectral component of the cavity voltage and the beam current for an LHC-type beam of 72 bunches at the nominal intensity required for the HL-LHC [12]. Following the calibration procedure described in [14], the shunt resistance with wideband feedback is calculated. During the acquisition, RF voltage manipulations are performed to reduce the bunch length of the beam to around 4 ns, according to the bunch rotation

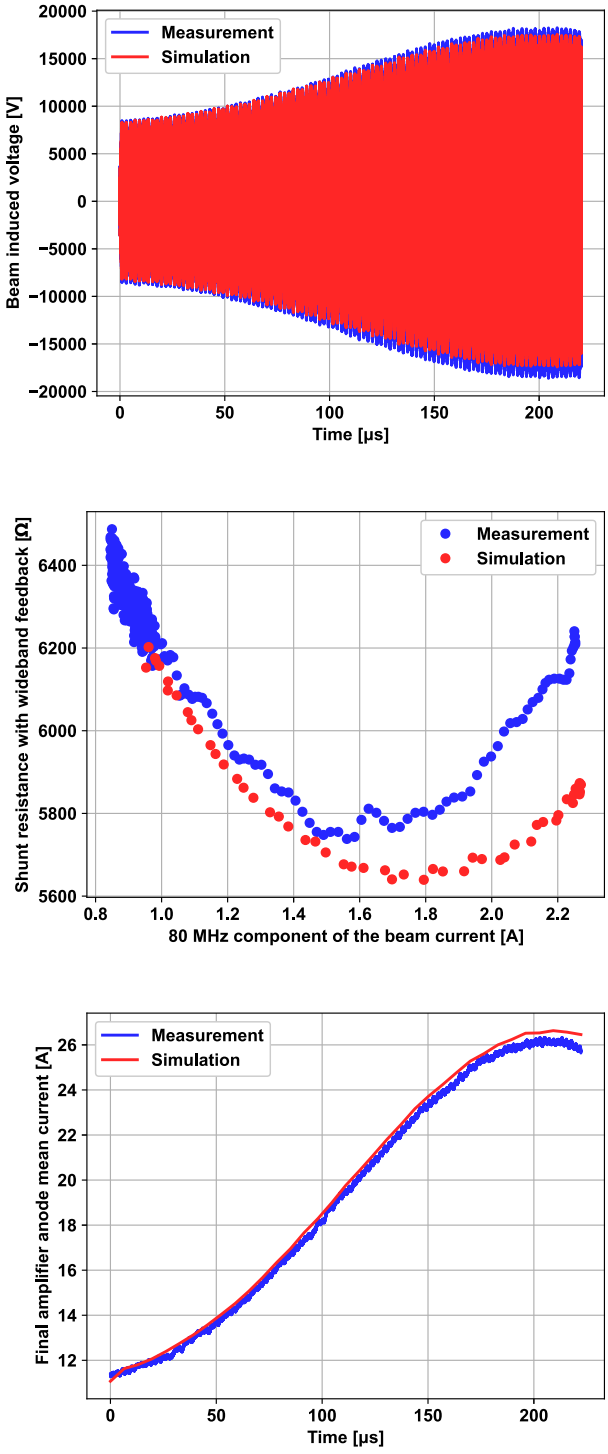


Fig. 15. Beam induced voltage in the cavity C80-88 (top), longitudinal beam coupling impedance (middle) and final amplifier anode DC current (bottom) observed during the bunch rotation. The model (red curves) correctly describes the measured behavior (blue curves), even when the system enters compression as indicated by the increase in impedance with the RF beam current.

program [28]. This increases the form factor of the beam [29]. This condition generates the highest beam induced voltage currently achievable in the cavity C80-88, and the highest steady state DC anode current of the final tube.

As demonstrated by the increase in impedance depicted in Fig. 15, this beam induced voltage is sufficient to reach the

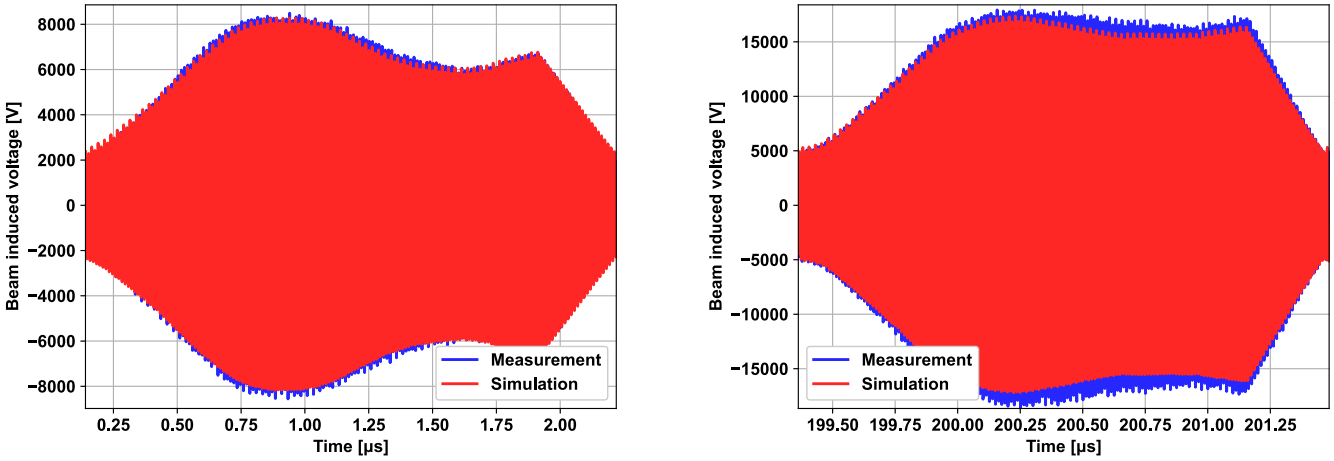


Fig. 16. Beam induced voltage in C80-88 before (left plot) and after (right plot) the bunch rotation.

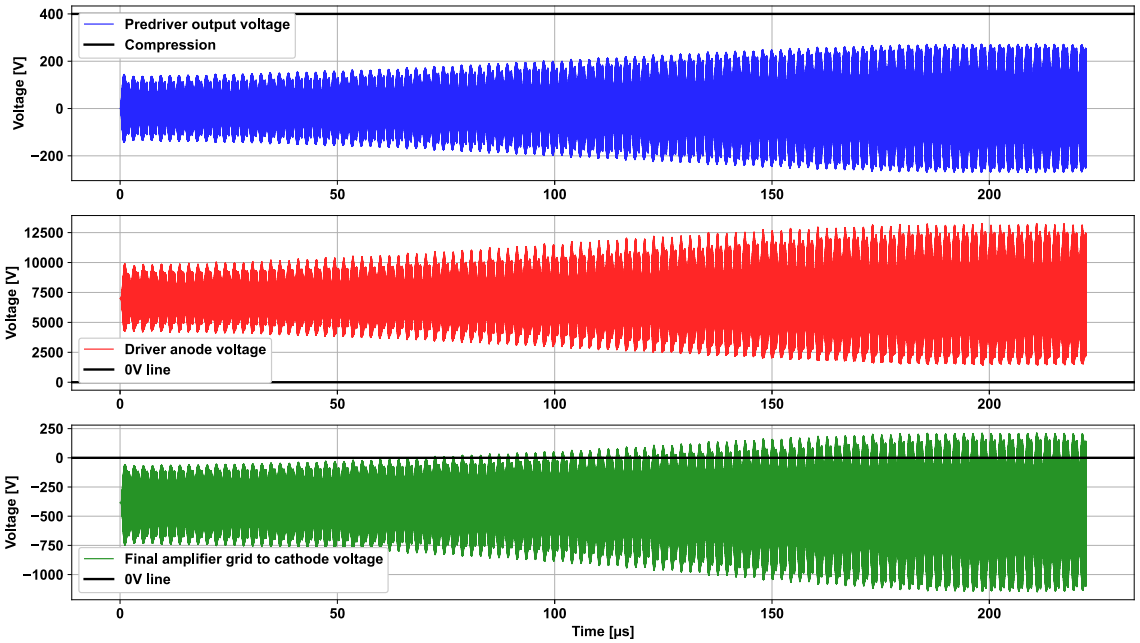


Fig. 17. Potential limitations of the RF system under beam loading conditions. The simulation of the pre-driver output voltage (blue curve) shows that it is operating below compression. The red curve shows that the anode voltage swing of the driver is becoming significant, especially for $I_b \approx 2.2$ A. The green curve shows that the final amplifier limits the gain of the amplifier chain, since current is drawn on the control grid when the grid to cathode voltage becomes positive.

RF system's limit. The measured time domain current has been used as an input to the cavity circuit, which allowed us to compare the measurements and the simulation up to the point where the RF system starts to enter compression. To match the 2024 configuration, the model's feedback gain was appropriately adjusted. In addition, a reduced tube current with respect to the nominal datasheet values was assumed in simulations in order to improve agreement with measurements. This reflects deviations from the datasheet tube characteristics under real operating conditions.

Fig. 15 shows that the model is able to reproduce the measurement of the impedance with good agreement, as the average RMSE is approximately 190 Ω over the measurement range. In addition, the model can replicate the measurements of the anode DC current and the cavity voltage, which were also acquired. The average RMSE of the anode DC current is 0.33 A.

Noticeably, the shape of the induced voltage waveform changes during the bunch rotation. Fig. 16, which is an enlarged view of the top plot of Fig. 15, at the beginning and at the end of the bunch shortening program, shows that the simulation is also able to reproduce this variation of the amplitude modulation with the RF beam current. The maximum error between the measured and simulated signals' voltage envelope is obtained at the end of the bunch rotation, and is lower than 10% of the measured envelope.

The model allows us to identify which element of the chain is responsible for the increase in impedance observed in the middle plot of Fig. 15. As it is shown in Fig. 17, the final amplifier's control grid voltage reaches positive values with respect to the cathode when the beam current becomes sufficiently high. Therefore, the control grid current increases and induces a drop in the grid voltage, thereby decreasing the gain of the amplifier and limiting the performance of

the chain. In addition, since the final amplifier control grid circuit was not designed to supply current, its hardware would have to be upgraded to operate with such beam loading. This could be combined with an optimization of the tube bias point, for instance by increasing the screen grid voltage while maintaining the same quiescent current, in order to reduce the control grid current and improve the large signal response. Moreover, it can be observed in Fig. 17 that there is not much margin left in the driver stage when the RF beam current reaches approximately 2.2 A due to its anode voltage drop. The simulation shows that the pre-driver can withstand the beam current as it is operating below the compression level represented in Fig. 4.

VI. Conclusion

A detailed circuit model was developed to study the beam-cavity interaction in a system made of a cavity and high-power amplifiers operating in the very high frequency (VHF) regime over their full power range.

The modeling of this complex system required different methods for the distinct parts of the amplifier chain. In particular, a new technique has been developed in order to model the vacuum tube based stages. The use of low- and high-power measurements together with a circuit optimizer allowed us to model the amplifier chain, including its stray and distributed components, as well as the nonlinear amplifier response to beam loading. This method allowed building a precise model, employed to identify the components limiting the performance of the chain under conditions of high beam loading and to explain the discrepancies between the different 80 MHz RF systems in the CERN PS.

The knowledge of the circuit topology is the only requirement of this technique. Hence, it can be extended to other configurations in which the beam-cavity interaction must be understood at beam intensities high enough to induce a nonlinear behavior of the amplification chain. As other RF systems in the PS present similar characteristics, the same approach will be applied to study their interaction with the beam.

Acknowledgment

The authors would like to thank the PS operators and Ben Woolley for their help in setting up the machine development beams and hardware settings.

References

[1] H.Damerau, "Radio-frequency (RF) systems," 2021, *arXiv:2108.06237*.

[2] T.Mastoridisand P.Baudrenghien, "CERN's super proton synchrotron 200 MHz cavity regulation upgrade: Modeling, design optimization, and performance estimation," *Phys. Rev. Accel. Beams*, vol. 25, no. 2, Feb.2022, Art. no. 021002.

[3] F.Tamura, "Multiharmonic vector RF voltage control for wideband cavities driven by vacuum tube amplifiers in a rapid cycling synchrotron," *Phys. Rev. Accel. Beams*, vol. 22, no. 9, Sep.2019, Art. no. 092001.

[4] N. V.Avreline, "The upgrade of the intermediate power amplifier of the TRIUMF 520 MeV cyclotron's RF system," in *Proc. 47th Eur. Microw. Conf. (EuMC)*, Nuremberg, Germany, Oct. 2017, pp. 856–859.

[5] B.Wu et al., "Operation analysis of high power tetrode tube for the wideband cavity in CSNS-II," *IEEE Trans. Nucl. Sci.*, vol. 70, no. 11, pp. 2388–2396, Nov.2023.

[6] J.Wu et al., "Analyzing vacuum tube operation for a wideband cavity using a circuit simulator," *IEEE Trans. Nucl. Sci.*, vol. 71, no. 11, pp. 2339–2349, Nov.2024.

[7] G.Favia et al., "The PS 10 MHz high level RF system upgrade," in *Proc. IPAC'16*, Jun. 2016, pp. 622–625.

[8] R.Garoby, "Beam loading in RF cavities," in *Proc. 4th U.S.-CERN School Part. Accel.*, Hilton Head Island, SC, USA, Nov. 1990, pp. 509–541.

[9] M.Benedikt, P.Collier, V.Mertens, J.Poole, and K.Schindl, "New PS RF cavities," *LHC Design Rep.*, vol. 3, pp. 55–64, Dec.2004.

[10] E. N.Shaposhnikova, E.Ciapala, and E.Montesinos, "Upgrade of the 200 MHz RF system in the CERN SPS," in *Proc. IPAC'11*, San Sebastian, Spain, Sep. 2011, pp. 214–216.

[11] D.Grier, E.Jensen, R.Losito, and A.Mitra, "The PS 80 MHz Cavities," in *Proc. EPAC'98*, Stockholm, Sweden, Aug. 1998, pp. 1773–1775.

[12] J.Coupard et al., "LHC injectors upgrade, technical design report," CERN, Geneva, Switzerland, Tech. Rep. CERN-ACC-2014-0337, Dec.2014.

[13] M.Meddahiand G.Rumolo, "Performance with the upgraded LHC injectors," in *Proc. IPAC'23*, Venice, Italy, Sep. 2023, pp. 1–6.

[14] M.Taquet et al., "Beam-cavity interaction in the CERN PS 80 MHz RF systems," in *Proc. IPAC'24*, Nashville, TN, USA, May 2024, pp. 3132–3135.

[15] F.Caspers, "RF engineering basic concepts: S-parameters," in *Proc. CAS-CERN Accel*. School, RF Accel., Ebeltoft, Denmark, Jun. 2011, pp. 67–94.

[16] D.Vondran, "Techniques for pulsed S-parameter measurements," *High Freq. Electron.*, vol. 2, no. 2, pp. 50–57, Mar.2003.

[17] *AWR Microwave Office*. Accessed: Nov. 10, 2025. [Online]. Available: https://www.cadence.com/enUS/home/resources/datasheets/awr-software-ds.html

[18] *PSpice*. Accessed: Nov. 10, 2025. [Online]. Available: https://www.pspice.com/

[19] K. R. Spangenberg, *Fundamentals of Electron Devices*. New York, NY, USA: McGraw-Hill, 1957.

[20] K. R.Spangenberg, *Vacuum Tubes*. New York, NY, USA: McGraw-Hill, 1948.

[21] G.Favia, "Study of the beam-cavity interaction in the CERN PS 10 MHz cavities and investigation of hardware solutions to reduce beam loading," *Ph.D. dissertation, Dept. Phys., Sapienza Univ.*, Rome, Italy, Feb.2017.

[22] W. J.Sarjeant, "Capacitor fundamentals," in *Proc. 19th Electr. Electron. Insul. Conf.*, Sep. 1989, pp. 1–51.

[23] A.Massariniand M. K.Kazimierczuk, "Self-capacitance of inductors," *IEEE Trans. Power Electron.*, vol. 12, no. 4, pp. 671–676, Jul.1997.

[24] J. L. B.Walker, *Handbook of RF and Microwave Power Amplifiers*. Cambridge, U.K.: Cambridge Univ. Press, 2011.

[25] Z. S.Bojkovic, B. M.Bakmaz, and M. R.Bakmaz, "Hamming window to the digital world," *Proc. IEEE*, vol. 105, no. 6, pp. 1185–1190, Jun. 2017.

[26] K. F.Anderson, "A survey of techniques for improving the calibration of high-power network analyzers," in *Proc. 78th ARFTG Microw. Meas. Conf.*, Dec. 2011, pp. 1–5.

[27] H.Wiedemann, *Particle Accelerator Physics*. Cham, Switzerland: Springer, Jul.2015.

[28] A.Lasheen, H.Damerau, J.Repond, M.Schwarz, and E. N.Shaposhnikova, "Improvement of the longitudinal beam transfer from PS to SPS at CERN," in *Proc. IPAC'18*, May 2018, pp. 3060–3063.

[29] P. F.Tavares, Å.Andersson, A.Hansson, and J.Breunlin, "Equilibrium bunch density distribution with passive harmonic cavities in a storage ring," *Phys. Rev. Special Topics-Accel. Beams*, vol. 17, no. 6, Jun.2014, Art. no. 064401.